Microstructure Evolution of Fine-Grained Heat-Affected Zone in Type IV Failure of P91 Welds

This work studies the precipitation behavior of Cr-rich $M_{23}C_6$ and MX carbonitrides and martensitic/ferritic grain evolution in FGHAZ of P91 welds over three thermal stages

BY Y. WANG AND L. LI

ABSTRACT

A microstructure analysis has been conducted on the fine-grained heat-affected zone (FGHAZ) of P91 welds that have undergone sequential thermomechanical histories: the as-welded (AW), after a postweld heat treatment, and after a creep rupture test. The Type IV failure is observed to have initiated by wedge-type cavities that coalesce to form an intergranular separation with a high local deformation at the outer edge of the FGHAZ. The ratio of the high-angle grain boundary (HAGB) frequency to low-angle grain boundary (LAGB) frequency in the FGHAZ increases from the as-welded 0.48 to the crept 1.06, resulting in an increased grain size from 1.2 μm (AW) to 3.1 μm (crept). The area fraction of the fully recrystallized ferrite grains increases from 14% (AW) to 45% (crept). Coarse, undissolved, Cr-rich $M_{23}C_6$-type carbides remain on prior austenite grain boundaries and packet/block boundaries after welding. V (C, N) and Nb (C, N) carbonitrides distribute at HAGBs. The MoC/Mo_2C and M_7C_3 precipitates form a grain boundary network that is believed to help the nucleation of cavities during creep. The kernel average misorientation (KAM) maps show the higher local strain level in the particle-containing grains. Straining variation of the particle-containing grains and particle-free grains in the crept FGHAZ can be traced back to the degree of austenitization in the welding thermal cycle. Creep deformation mismatch between fully recrystallized grains that are free of precipitates and the unrecrystallized grains that contain carbide particles seems to have contributed to nucleation of the initial creep cavities.

KEYWORDS

• P91 Steel • Electron Back-Scatter Diffraction (EBSD)
• Fine-Grained Heat-Affected Zone (FGHAZ) • Microstructure • Type IV Creep Rupture

Introduction

P91 steel, known as modified 9Cr-1Mo-V-Nb steel (ASTM A335 P91 for pipe), has been widely used for pressure vessels and superheaters in fossil fuel power plants due to its high corrosion resistance and creep resistance (Refs. 1–3). The as-received P91 steel is usually normalized at 1038°–1149°C and tempered at a minimum temperature of 732°C (Ref. 4). The microstructure of the P91 base metal is reported to consist of tempered martensite and dispersed carbides/carbonitrides at the prior austenite grain boundaries (PAGBs) and martensite lath/packet boundaries (Refs. 4–6). The 10,000-hour lifetime rupture strength of P91 steel can be 200 MPa at 500°C (Ref. 7). However, creep strength of P91 welds dramatically decreases due to the non-equilibrium structure of the heat-affected zone (HAZ) caused by exposure to various peak temperatures and high heating and cooling rates in the welding thermal cycles. The HAZ of a P91 weld is divided into coarse-grained HAZ (CGHAZ, $T_p >> A_{C3}$), fine-grained HAZ (FGHAZ, $T_p > A_{C3}$), and intercritical HAZ (ICHAZ, $A_{C3} > T_p > A_{C1}$) based on the prior austenite grain size in various peak temperatures (Refs. 8, 9).

Figure 1 shows typical heat-affected zone regions and their dimensions in a 25-mm-thick P91 pipe joint, fusion welded using a matching flux-cored wire. The microstructure of the ICHAZ (Fig. 1D) shows a mixture of fine grains formed during welding thermal cycle and coarser grains retained from the base metal.

Several factors contribute to the long-term creep performance of P91 welds, including chemical composition of base metal and filling materials, joint design, welding procedure, and heat treatment. In the lifetime of a P91 weld, it experiences three thermal stages, including the as-welded (AW), postweld heat treated (PWHT), and high-temperature service exposed (crept). Many researchers have investigated the microstructure of welds at the individual thermal stage. To the knowledge of the authors, no researcher has studied a given set of welds and tracked their microstructure evolution for all three stages.

The relatively low peak temperature (just above A_{c3}) and short dwell time in the FGHAZ during the welding thermal cycle are believed to limit the grain growth after diffusive α/γ transformation and dissolution of coarse precipitate particles. This low peak temperature produces the fine prior austenite

Y. WANG is a PhD candidate and L. LI (leijun@ualberta.ca) *is a professor with the Department of Chemical and Materials Engineering, University of Alberta, Edmonton, AB, Canada.*

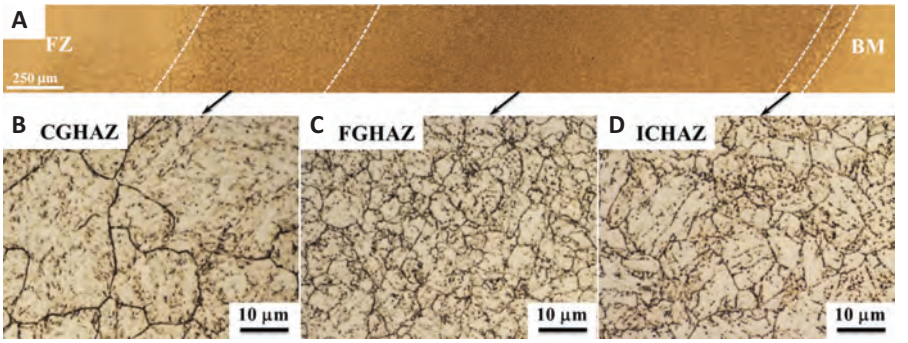

Fig. 1 — Microstructure of the heat-affected zone (HAZ) in the as-welded P91 specimen (10% Nital etched). A — Overview of the HAZ from the fusion zone (FZ) to the base metal (BM); B — coarse-grained HAZ (CGHAZ); C — fine-grained HAZ (FGHAZ); D — intercritical HAZ (ICHAZ).

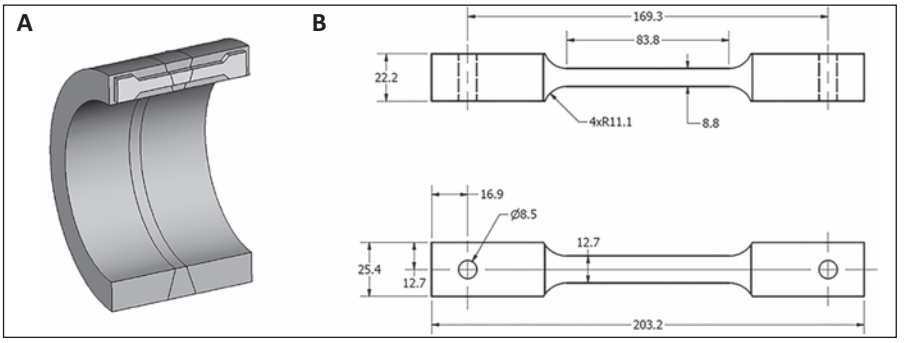

Fig. 2 — A — Schematic of cross-weld creep test specimen extracted from the welded pipe after PWHT; B — the dimensions of the creep rupture specimen (in mm).

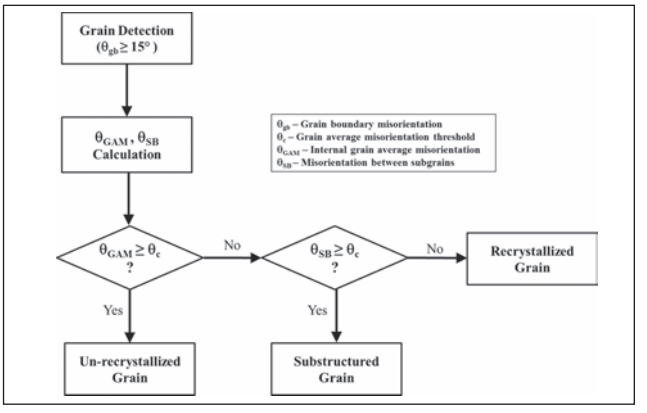

Fig. 3 — The logic flow for deciding whether a grain is recrystallized, contains subgrains, or is deformed is found by comparing the grain average misorientation (GAM) with a threshold of 1.0 deg.

grains and undissolved particles in the FGHAZ (Ref. 10). Sawada et al. (Ref. 11) have reported a martensitic structure with very fine laths that contain a high dislocation density in the FGHAZ of modified 9Cr-1Mo steel weld. Undissolved $M_{23}C_6$ and V-Nb MX particles are detected at the grain boundaries of the FGHAZ. Paddea et al. (Ref. 12) reported FGHAZ has a high tensile residual stress because of the strength mismatch between the base metal and fusion zone. The highest tensile residual stress of 600 MPa is located at the boundary of HAZ and adjacent base metals, and a decreased tensile residual stress of 120 MPa still remains in the vicinity of the HAZ after PWHT.

Postweld heat treatment at a temperature below the A_{c1} temperature is required to reduce the residual stresses and to temper the fresh martensite. During PWHT, recovery and dynamic recrystallization of the martensite laths along with coarsening and redistribution of precipitates are observed in HAZ. It is reported that the hardness in FGHAZ close to the base metal decreases faster due to a higher annihilation rate of excess dislocations during PWHT (Ref. 13). Liu et al. (Ref. 14) found that the equiaxed grains in the FGHAZ after PWHT are free of dislocations, resulting in the distribution of carbides/carbonitrides on the PAGBs and block boundaries.

The microstructure evolution of martensite laths and precipitates in the FGHAZ is reported to determine the creep behavior of P91 welds (Refs. 15–18). The complex microstructure evolution of P91 welds during creep is associated with the recovery and recrystallization of martensite laths and the coarsening and redistribution of precipitates. As a premature failure mode of welded P91, the typical Type IV creep rupture occurs in the transition zone between the FGHAZ and the ICHAZ (Refs. 19, 20). The Type IV rupture is considered brittle because of a small total creep deformation at failure. The nucleation and growth of cavities in the FGHAZ/ICHAZ are reported as the main mechanism of the intergranular fracture of P91 welds during creep (Ref. 21). Coarse $M_{23}C_6$ particles on the PAGBs, especially on the intersection of grain boundaries, are suggested as the preferential nucleation sites for cavities (Refs. 10, 11). The grain growth of the newly recrystallized grains and coarsening of $M_{23}C_6$ carbides are reported to be accelerated by the applied stress during creep (Ref. 22).

Parker et al. (Refs. 23, 24) report that a local band, free of martensitic transformation, within the FGHAZ/ICHAZ, leads to a local high residual stress, which is responsible for the Type IV failure of P91 welds. AbdEl-Azim et al. (Ref. 25) have investigated the microstructural instability of FGHAZ of P91 welds after PWHT and long-term creep at 650°C and concluded that the prior austenite grain size (PAGS) is the main factor that affects the creep behavior of the welds. They further point out that the finer the PAGS, as observed in the FGHAZ, the higher the recovery rate of excess dislocations, which leads to higher rates of subgrain growth and precipitate coarsening.

On the other hand, Liu et al. (Ref. 26) have reported that the fine-grained microstructure in the FGHAZ is not directly responsible for the Type IV failure. They believe that the precipitate formation behavior at PAGBs and

lath/block boundaries is the critical factor. Boundary strengthening by precipitates plays the most important role in preventing Type IV failure of the welds. They proposed a boundary-strengthening method by addition of boron alloying elements. Boron promotes precipitate formation not only at PAGBs, but also along the lath/block boundaries, which helps to stabilize the microstructure of HAZ and prolong the creep lifetime of the welds.

The objective of this work is to study the precipitation behavior of Cr-rich $M_{23}C_6$ carbide and MX carbonitrides, and martensitic/ferritic grain evolution in FGHAZ of P91 weld in three sequential thermal stages, consisting of the as-welded, after PWHT, and after creep test. This work summarizes the evolution of FGHAZ microstructure in Type IV creep rupture of P91 welds, including matrix grain size, grain boundary types, precipitate type, size, and distribution.

Materials and Experimental Procedure

Materials and Welding Process

The P91 steel pipe used as the base material had a 219-mm (8.625-in.) outer diameter (OD) and 29-mm (1.143-in.) thickness. It had been normalized for 8 min at 1060°C and tempered for 45 min at 786°C. Flux cored arc welding (FCAW) and gas tungsten arc welding (GTAW) were used to weld two 124-mm-long pipes with a 60-deg double-V weld groove and 1.5-mm root face, respectively. Chemical compositions of P91 base material, GTAW filler metal ER90S-B9 (1.2-mm diameter) and FCAW filler metal ER91T1-B9 (1.2-mm diameter) are presented in Table 1.

Gas tungsten arc welding parameters used for the root pass were 300 A DC and 1.27 m/min wire feed speed. FCAW parameters for the filling passes were 26.1- and 27-arc voltage and 6.35 and 7.62 m/min wire feed speed. A stepper motor-controlled fixture was used to maintain 0.14 m/min linear travel speed. A preheat temperature of 150°C, an interpass temperature of 300°C, and a wire feed speed of 7620 mm/min at 27 V were selected. Shielding gases used for GTAW and FCAW were pure argon and mixed 75/25 argon/CO_2, respectively. For hydrogen bake-out, a postweld isothermal hold was conducted at 250°C for 4 h. Postweld heat treatment of the weld was performed in a Cress electric furnace Model C162012/SD. The PWHT parameter is the code recommended following ASME B31.1 — 760°C for 2 h.

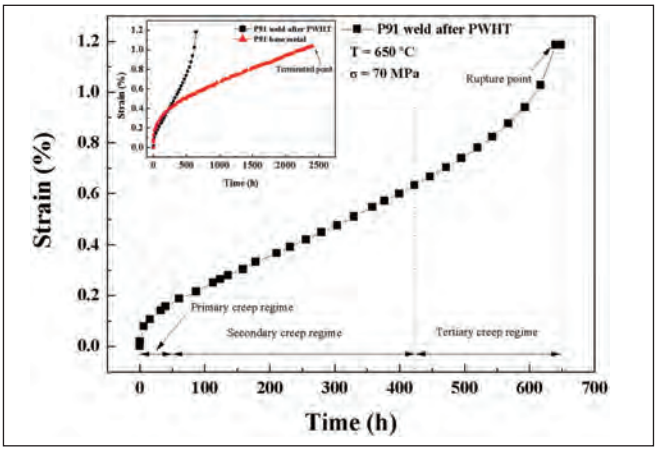

Fig. 4 — Creep curves of the P91 cross-weld specimen after PWHT (760°C for 2 h) and the as-received base metal. Creep tests were performed at 650°C with a stress level of 70 MPa. The test of the as-received base metal was terminated in the secondary creep regime. Creep rupture occurred in one HAZ of the cross-weld specimen. The other HAZ (not ruptured but contained cavitation damages) was used for the post-test evaluations.

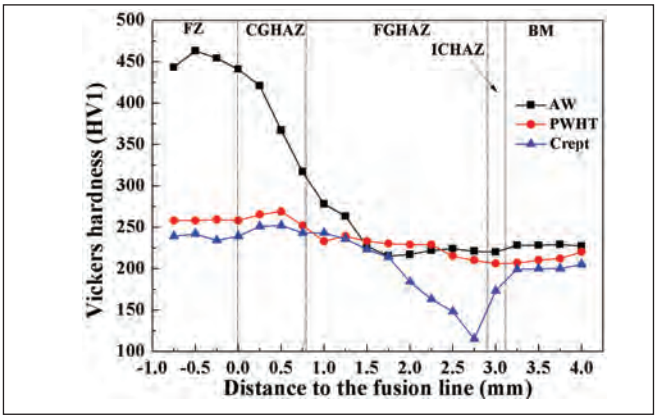

Fig. 5 — Microhardness across the P91 weld joint in three thermo-mechanical conditions. The criteria for the CG/FG and FG/IC boundaries are determined by grain size measurements.

Mechanical Property and Microstructure Characterization

Creep tests were performed on the P91 weld joint after PWHT and the as-received base metal. A cross-weld specimen for creep test was extracted from the center of the weld after PWHT. This cross-weld specimen includes FCAW weld metal, and HAZs on both sides of the weld metal and the base metal. The rectangular cross-section creep specimen had a cross section of 8.8 × 12.7 mm and an effective gauge length of 84 mm, shown in Fig. 2. The creep test was conducted at applied test temperature of 650°C and engineering stress of 70 MPa (10 ksi). The creep test procedure was conducted following the standard test procedures guided by ASTM E139-06 (Ref. 27).

Vickers hardness across the cross-section of polished welds was measured with 1 kgf and a dwell time of 10 s by using a Tukon 2500 automated hardness tester. For microstructure characterization, six specimens from

Table 1 — Chemical Composition of Grade 91 Base Material and Filler Metals (wt-%)

Materials	C	Cr	Mo	Mn	Si	Ni	Al	V	Nb	S	P	N
ER90S-B9 GTAW	0.097	8.830	0.928	0.560	0.250	0.307	0.002	0.197	0.064	0.004	0.006	0.030
E91T1-B9 FCAW	0.100	8.830	0.880	0.790	0.280	0.550	0.001	0.200	0.030	0.008	0.020	0.050
Base Metal	0.110	8.470	0.940	0.370	0.370	0.080	0.002	0.190	0.071	0.002	0.016	0.048

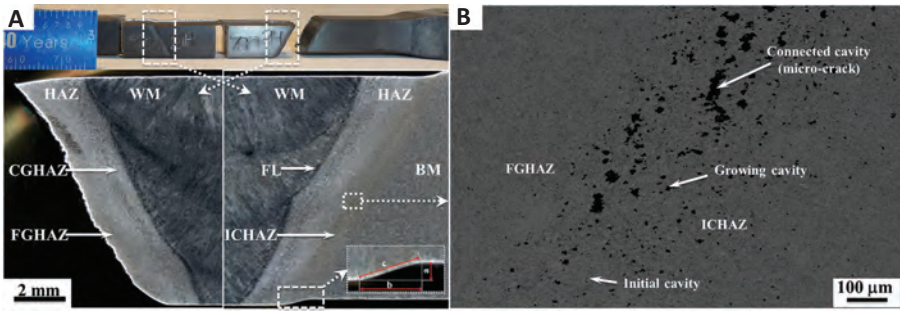

Fig. 6 — Typical Type IV failure of the cross-sectional weld after creep test. A — Macrostructure of the ruptured weld; B — backscattered electron (BSE) image of the failed transition zone between FGHAZ and ICHAZ indicates the three-stage lifetime of the cavity: initial cavity, growing cavity, and connected cavity.

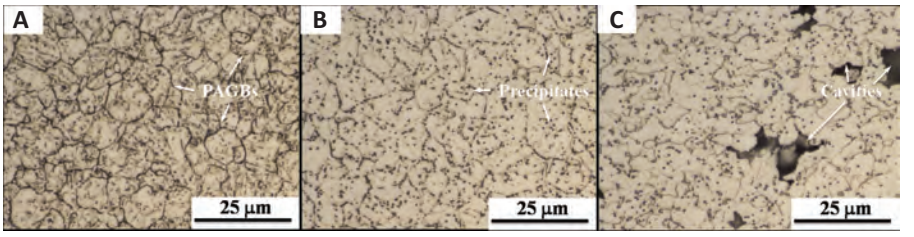

Fig. 7 — Micrographs of FGHAZ in three thermal conditions. A — As-welded; B — after PWHT; C — after creep test.

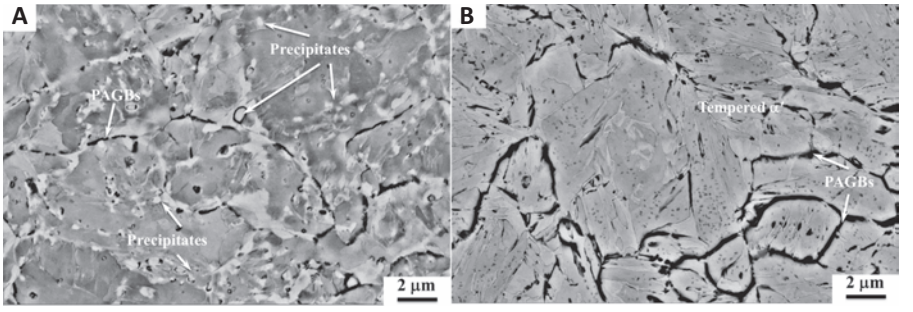

Fig. 8 — A — Backscattered electron (BSE) images of the as-welded FGHAZ; B — deep etched with 10% Nital to show the prior austenitic grain boundaries (PAGBs).

HAZ were cut from the three thermal conditions, as-welded (AW), after postweld heat treatment (PWHT), and after creep test (crept). These specimens were mounted, ground, and polished by using a conventional mechanical polishing method. Grit #360, #600, #1200 SiC sandpapers were used for grinding. Three-μm and 1-μm diamond suspension, 0.5-μm and 0.05-μm alumina suspension, and 0.02-μm colloidal silica were used for polishing. Electron backscatter diffraction (EBSD) analysis on FGHAZ was conducted on two specimens for each test condition by using a Zeiss Sigma field-emission SEM (FESEM) equipped with an Oxford AZtec system under 20-kV accelerate voltage, and 60-μm objective aperture. A spot size of 10 nm and step size of 0.15, 0.10, and 0.13 μm were used in EBSD for AW, PWHT, and crept specimens, respectively.

The EBSD-analyzed areas for each test condition were 390 μm^2 (as-welded), 390 μm^2 (PWHT), and 1049 μm^2 (crept). The increase in the area for the crept samples was to make sure a comparable number of grains was analyzed, as there was significant grain growth in the crept samples. Specimens for EBSD characterization were in as-polished condition without etching. The polished specimens for optical and FESEM microscope analysis were etched with 10% Nital for 2 to 10 min.

Phase identification and orientation relationship of the matrix grains and precipitates were analyzed by EBSD with Oxford AZtec software.

Postprocessing EBSD data was conducted by using a Channel 5 software package. Phase distribution maps were created based on the indexed Kikuchi patterns. The area fraction of the precipitates was calculated according to the indexed pixels. Matrix grain orientation was presented by the inverse pole figure (IPF) in Z [001] direction (perpendicular to the screen). Low-angle grain boundaries (LAGB, misorientation θ between 2 and 15 deg) and high-angle grain boundaries (HAGB, misorientation θ > 15 deg) were distinguished by the scalar misorientation between adjacent pixels. Local misorientation maps were processed by calculating kernel average misorientation (KAM) between all pixels of a kernel (Refs. 28–30). The KAM value will be relatively larger if the calculated kernel contains a grain boundary. A higher local misorientation correlates with a higher local strain and deformation. Grain average misorientation (GAM) with a threshold (θ_c) was used to quantitatively distinguish the unrecrystallized grain and recrystallized grains. The GAM is the average misorientation between each neighboring pair of the measured pixels within each grain, which evaluates the local strain of individual grain (Refs. 27, 28). The GAM is calculated as follows (Ref. 31):

$$GAM = \frac{1}{N}\frac{1}{n}\sum_{j=1}^{N}\sum_{i=1}^{n}\theta_{ji}\left(j \neq i\right) \qquad (1)$$

where N is the number of pixels in a grain, n is the number of neighboring pixels, and θ_{ji} is the misorientation between the measured pixel j and neighboring pixel i. It is proved that GAM provides a reliable measurement of recrystallized grains (Refs. 32, 33). In this study, the recrystallized fraction of grains in the FGHAZ was evaluated by using GAM with a commonly used threshold (θ_c) of 1.0 deg.

The logic flow for classification of the grains is shown in Fig. 3. The internal average misorientation angle within the grain and misorientation between subgrains was measured to categorize the grains. The grain with an internal grain average misorientation (θ_{GAM}) higher than the threshold (θ_c) is defined as an "unrecrystallized grain." When the θ_{GAM} of the grain is lower than the threshold (θ_c), but the misorientation between the subgrains (θ_{SB}) is higher

than threshold (θ_c), this grain is classified as a "substructured grain" or "partially recrystallized grain." The grain with θ_{GAM} lower than the threshold (θ_c) or subgrain misorientation lower than the threshold (θ_c) or without subgrains is defined as a "recrystallized grain."

Experimental Results

Creep Test and Microhardness

Figure 4 shows creep curves of the P91 cross-weld specimen after PWHT and the as-received base metal tested at 650°C with a stress level of 70 MPa. The creep curve of the P91 cross-weld shows a typical three-stage curve, including primary creep regime, secondary creep regime, and tertiary creep regime. The primary creep regime of base metal is much longer than that of the weld. The curve of the weld shows it quickly enters the secondary creep regime with a constant strain rate. In the tertiary creep regime, the cavities promote the rapid deformation of the weld with an increasing strain rate. The weld ruptured at testing time 649 h with an average tensile strain of 1.2% over the entire gauge length. The test of the as-received base metal was terminated in the secondary creep regime at 2402 h with an average tensile strain of 1.0% over the entire gauge section. It is obvious that the creep rupture strength of the weld is much lower than that of the base metal.

Microhardness traverse distribution as affected by the thermal histories is shown in Fig. 5. Hardness of all regions decreased after PWHT and the creep test. The fusion zone shows the highest hardness, 463 HV1, in the AW condition due to untempered martensite formed following weld cooling. Hardness in AW-CGHAZ gradually decreases along with the gradient peak temperature (above A_{C3}) and cooling rate during the welding process. The FGHAZ is the softest region, with a hardness value of 220 HV1 for AW, 206 HV1 for PWHT, and 115 HV1 for the crept condition, respectively.

Figure 6 shows a typical Type IV creep rupture of the cross-weld P91 joint tested at 650°C with a stress level of 70 MPa. Failure of the weld joint occurred in the outer edge of the FGHAZ and ICHAZ close to base metal. The weld metal, much of the HAZ, and the base metal show no large plastic deformation during creep. The plastic deformation (shown as the shear-deformed steps in Fig. 6A) was observed at a region 0.5 mm wide, located near the outer edge of the HAZ, where the creep cavity concentrated — Fig. 6B. Because of the creep strength variation between fusion zone and base metal, a shear deformation occurred during creep test. Failure of the weld is caused by the formation of the cavities in the shear deformation zone. The cavity damage is observed to have started in the middle thickness of the

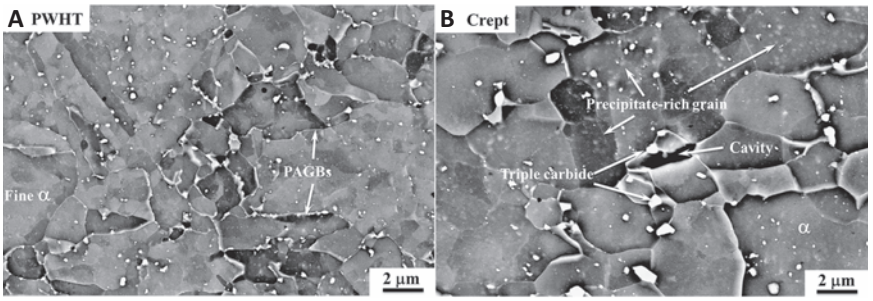

Fig. 9 — A — Backscattered electron (BSE) images of FGHAZ following PWHT; B — following creep rupture (10% Nital etch).

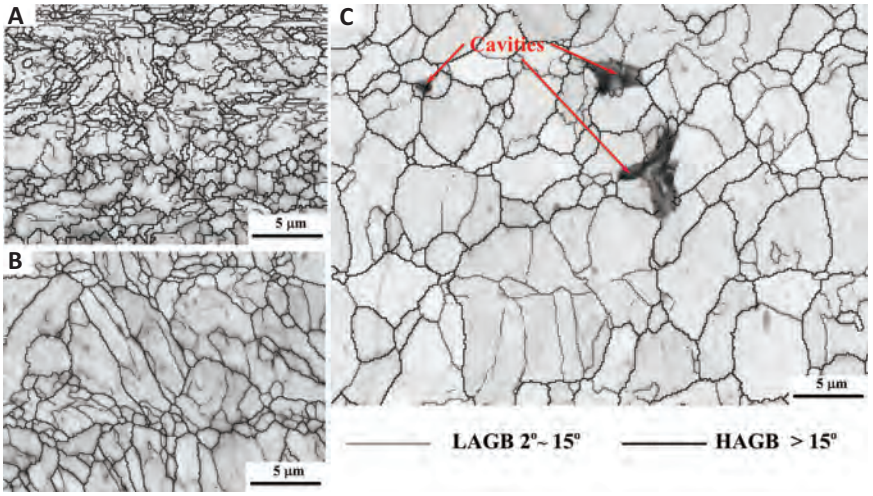

Fig. 10 — High-angle grain boundary (HAGB) and low-angle grain boundary (LAGB) distributions in FGHAZ. A — In the as-welded; B — postweld heat-treated; C — creep rupture tested (dark lines indicate HAGB, misorientation > 15 deg, light lines indicate LAGB, misorientation = 2~15 deg, cavities are marked by arrows).

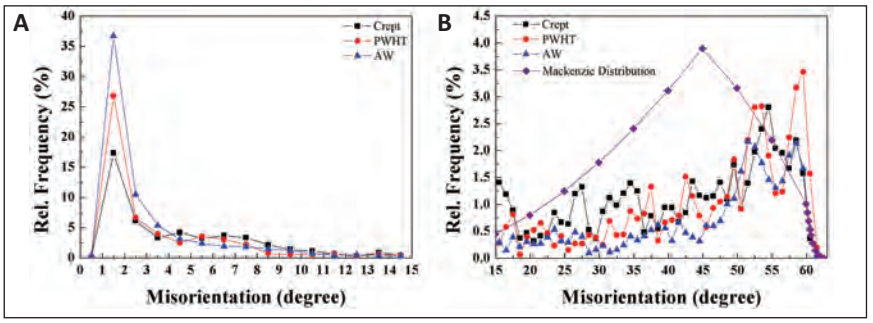

Fig. 11 — Relative frequency distribution of grain boundary misorientation in FGHAZ. A — Misorientation range from 0 to 15 deg; B — misorientation range from 15 to 62.8 deg. As-welded FGHAZ (red circle and line), PWHT FGHAZ (blue triangle and line, and crept FGHAZ (black cubic and line). Mackenzie distribution for random misorientation is also shown in B.

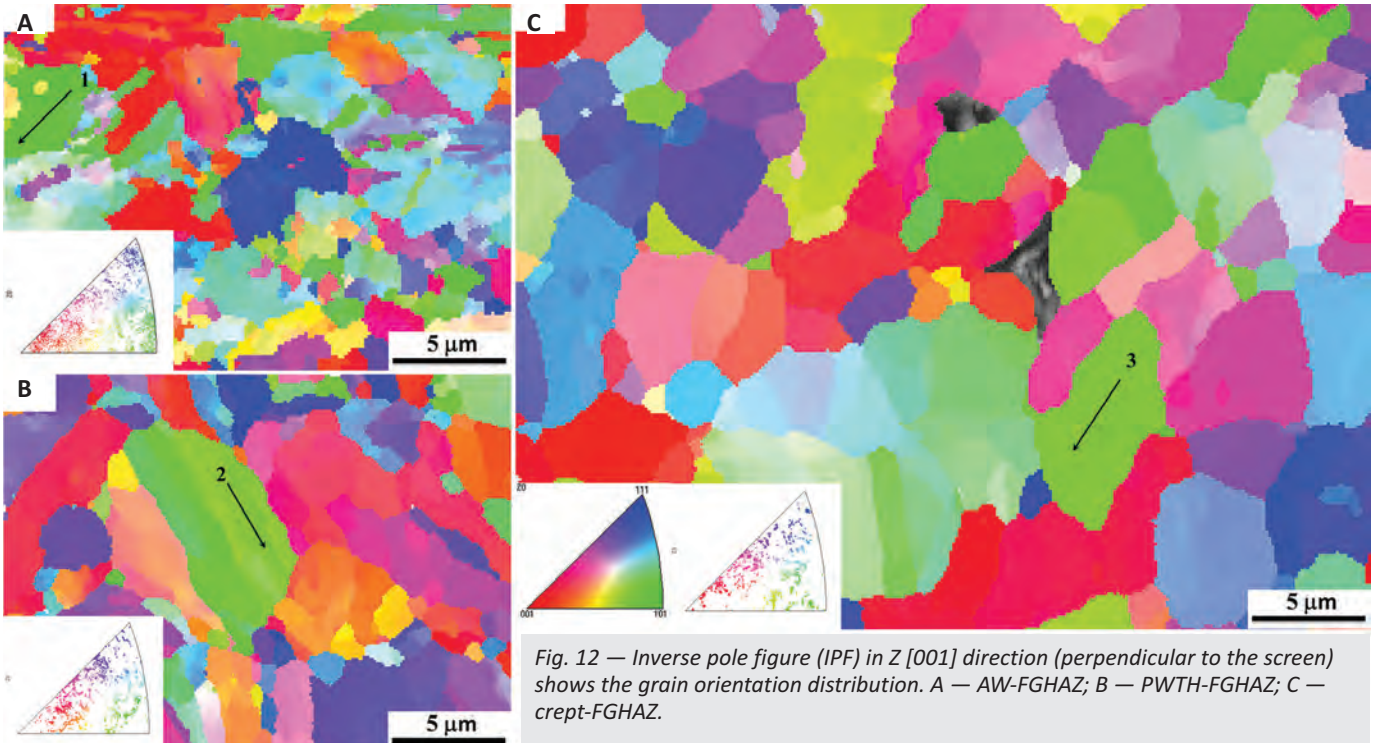

Fig. 12 — Inverse pole figure (IPF) in Z [001] direction (perpendicular to the screen) shows the grain orientation distribution. A — AW-FGHAZ; B — PWTH-FGHAZ; C — crept-FGHAZ.

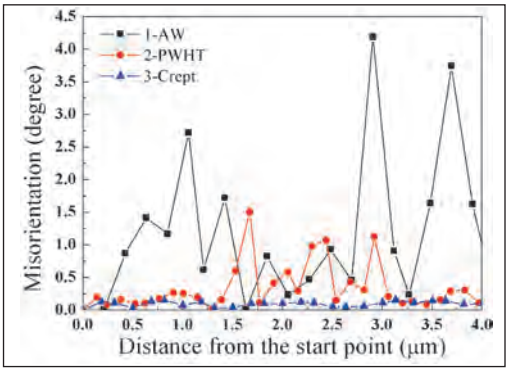

Fig. 13 — Neighboring misorientation profiles within the grains marked in Fig. 12 (the start point is the origin of the arrow).

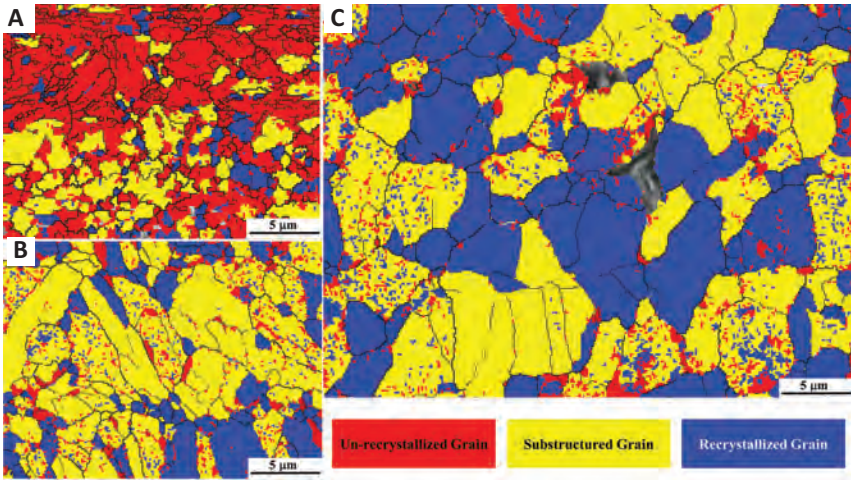

Fig. 14 — Recovery and recrystallization in FGHAZ. A — AW; B — PWHT; C — crept. Colors for uncrystallized grains (red), substructured/partially recrystallized grain (yellow), and recrystallized grain (blue).

cross-weld specimen. Figure 6B presents the three-stage lifetime of cavities, which includes initial cavities, growing cavities, and connected cavities. The connected cavities promote the generation and propagation of the microcracks, which reduces the creep strength of the weld. Creep strain (shear strain) is mostly concentrated at the narrow Type IV damage zone. The local strain (tensile strain and shear strain) of 8.0% in the damage zone marked by the rectangle at the right bottom of the specimen is estimated by measuring the "boxed" shear-deformed step in Fig. 6A. This estimated local strain near the shear steps, measured as

$$(c-b)/b=\left(\sqrt{a^2+b^2}-b\right)/b$$

in Fig. 6A, is much higher than the average tensile strain of 1.2% over the entire gauge length, measured at rupture of the specimen. The resolved shear and tensile strains, as affected by the groove angle of the weld joint, have significant effects on creep rupture of P91 cross-weld specimens (Refs. 23, 24).

Evolution of FGHAZ Microstructure

Figure 7 shows the microstructure evolution of FGHAZ in three thermal stages. Martensitic substructure can be observed within the prior austenite grains (PAGs) in the as-welded condition. Dark dots along PAGBs or within the PAGs are carbides or carbonitrides. Compared with precipitates in AW condition, the carbide particles coarsen during the PWHT, and redistribute

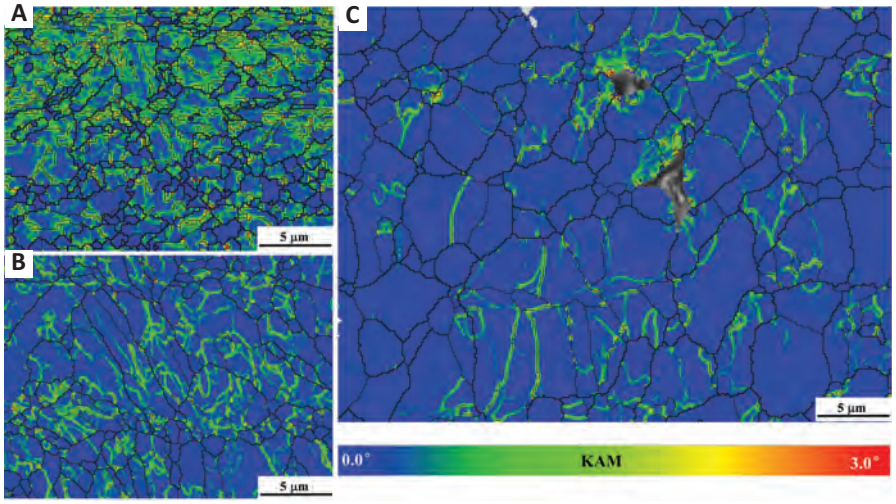

Fig. 15 — Overlapping of local misorientation (KAM) map and grain boundary map of FGHAZ shows the high strain level in AW condition and neighboring grains around cavities. A — AW; B — PWHT; C — crept.

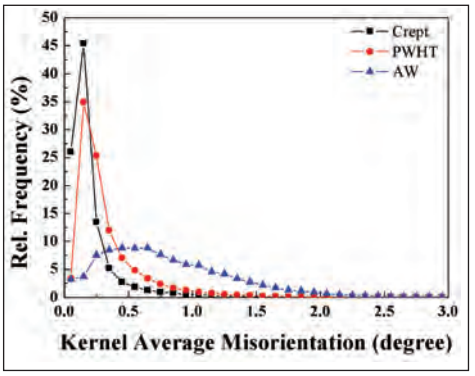

Fig. 16 — Kernel average misorientation (KAM) distributions of FGHAZ in three thermal stages.

along the PAGBs and subgrain boundaries — Fig. 7B. After creep test, the precipitates grow even bigger and redistribute along PAGBs and within the subgrains — Figs. 7C, 9B. All wedge-type cavities are observed along the PAGBs.

Backscattered electron (BSE) images in Fig. 8 reveal more structural details of the as-welded FGHAZ. Fine and coarse precipitates are distributed on PAGBs and subgrain boundaries. Deep-etched FGHAZ in Fig. 8B clearly shows the short martensite laths within PAGs. Fine precipitates distribute within the martensite laths or on lath boundaries. After PWHT, the lath martensite substructure is tempered and decomposed into a fine equiaxed ferrite — Fig. 9A. PAGBs with coarse precipitates are still visible. Coarse precipitates stay at the former martensite lath boundaries. Finer particles precipitate within the equiaxed subgrains. Following further tempering and accumulated strain during creep test, larger equiaxed grains are observed — Fig. 9B. Some coarse precipitates lie at the triple points of grain boundaries. PAGBs are not clearly revealed due the migration of the grain boundaries during recrystallization and grain growth. Fine precipitates concentrate in some particular grains, but not in all grains. The wedge-type cavity forms on those grain boundaries with dispersed coarse precipitates. It must be pointed out that the current discussion is based on distributions of precipitates detectable by FESEM and EBSD (such as in Fig. 9), and the effects of precipitates smaller than 0.1 μm are not considered.

Low-angle grain boundaries (LAGB, with a misorientation of 2 to 15 deg) and high-angle grain boundaries (HAGB, with a misorientation > 15 deg) of the matrix grains in FGHAZ were classified by measuring the misorientation between adjacent grains — Fig. 10. Subgrain boundaries, such as lath and block/packet boundaries within PAGs, have lower misorientation than that of PAGBs. PAGBs are identified as HAGBs due to their higher misorientation. In the as-welded condition, the tempered martensite substructure obtains more LAGBs — Fig. 10A. After PWHT, recovery and recrystallization of the martensitic grains result in more HAGBs — Fig. 10B. When creep test is performed, grain growth and further recrystallization contribute to even more HAGBs — Fig. 10C.

Misorientation distribution of the grain boundaries in FGHAZ is shown in Fig. 11. Misorientation distribution peaks of HAGBs in FGHAZ shift from 45 deg in the Mackenzie distribution of randomly misoriented grains to 50~60 deg due the recovery and recrystallization effects shown in Fig. 11B.

Relative frequency of LAGB and HAGB is calculated and presented in Table 2. The ratio of HAGB/LAGB increases from 0.48 to 0.88 and 1.06. Fine lath-shaped subgrains are observed in AW-FGHAZ. Coarse lath-shaped grains and fine equiaxed grains are the characteristic grains of PWHT-FGHAZ. Crept-FGHAZ shows coarse equiaxed grains. The average grain sizes, determined by the line intercept procedure of ASTM E211, of the matrix grains are shown in Table 2. The as-welded FGHAZ has the smallest average grain size of 1.2 μm. After PWHT, the FGHAZ has a slightly increased average grain size of 1.8 μm. After creep test, the FGHAZ has a significantly increased grain size of 3.1 μm.

The inverse pole figure (IPF) in Z [001] direction (perpendicular to the

Table 2 — Grain Size, Phase, GB, and Grain Distribution of FGHAZ in Three Thermal Histories

Specimen Condition	Ferrite		Area Fraction (%) of Phases		GB Frequency (%)		Ratio of HAGB/LAGB	Area Fraction (%) of Ferrite		
	Grain Size μm	Standard Deviation	Fe-bcc/bct	Precipitates	HAGB (>15 deg)	LAGB (2~15 deg)		Recrystallized	Substructured	Unrecrystallized
AW	1.2	1.14	88.5	11.5	32.4	67.6	0.48	14.3	45.0	40.7
PWHT	1.8	0.94	88.9	11.1	46.7	53.3	0.88	27.0	68.1	4.9
Crept	3.1	2.67	88.7	11.3	51.5	48.5	1.06	45.1	50.8	3.1

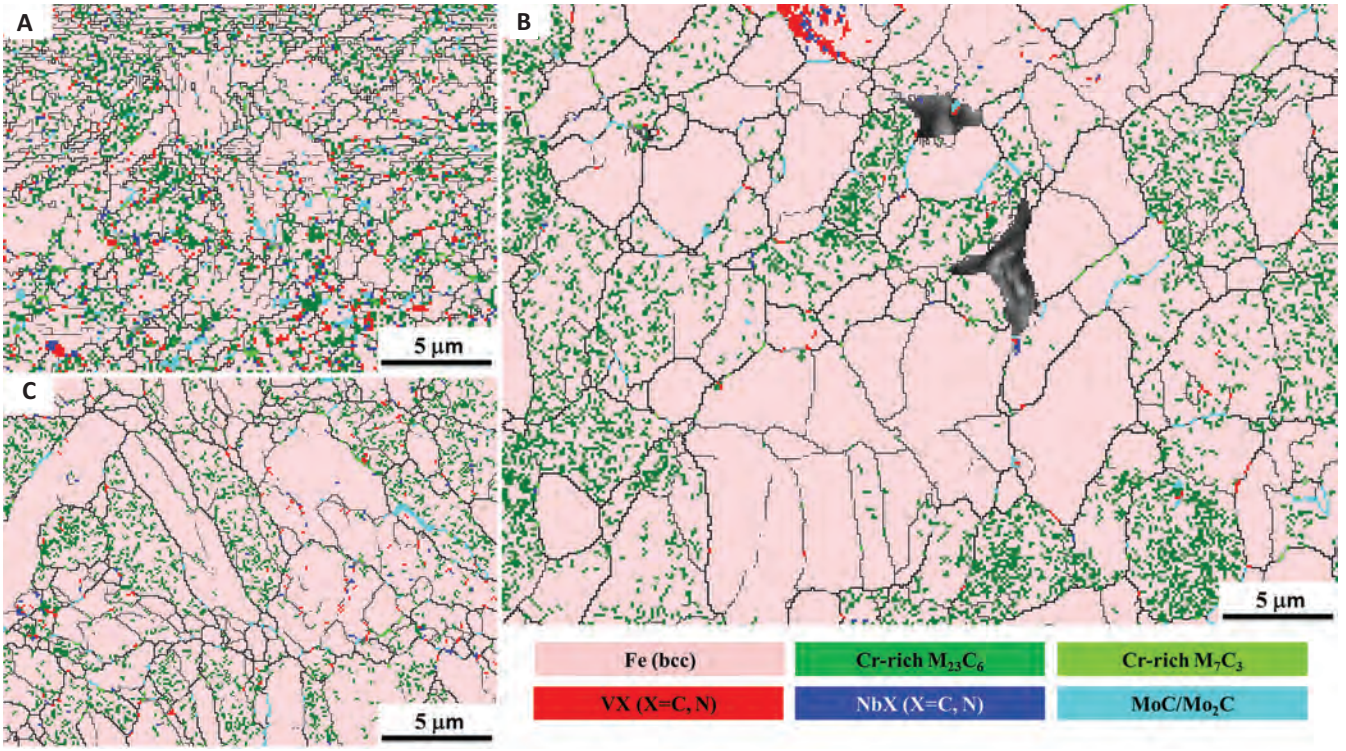

Fig. 17 — Overlapping of EBSD phase map and grain boundary map of FGHAZ show coarsening and segregation of the precipitates, especially $M_{23}C_6$ carbides in AW, PWHT, and crept conditions. A — AW; B — PWHT; C — crept. Phases show as different color symbols. Martensite and ferrite are processed as the same phase background color in pink.

screen) in Fig. 12 shows the grain orientation distribution in FGHAZ. A legend in Fig. 12C illustrates different orientations in different colors. The as-welded FGHAZ shows the largest grain orientation variation due to fine nucleated grains. Because of the recovery and recrystallization of the matrix grains after PWHT, a relatively lower grain orientation variation is observed in PWHT-FGHAZ. Crept-FGHAZ has the lowest grain orientation variation due to the highly recrystallized grains.

The misorientation profiles in Fig. 13 are calculated based on the neighboring pixels across grains with similar orientation in three thermal stages. It clearly shows the grain in the AW condition has the highest misorientation (> 4.0 deg), which indicates its greater crystal distortion. In the PWHT condition, the highest misorientation in the FGHAZ is 1.5 deg. In the crept condition, the FGHAZ shows the lowest misorientation (0.1 deg).

Distribution of the unrecrystallized grains, substructured, and recrystallized grains, including precipitates, is shown in Fig. 14. The area fraction for each of the three kinds of matrix grains is calculated and tabulated in Table 2. It is notable that the relative fraction of carbides remains a constant during the evolution of the microstructure, although their sizes and distributions will change. In the as-welded condition, the FGHAZ has the highest fraction of unrecrystallized grains (28.5%) and the lowest fraction of recrystallized grains (4.9%). On the contrary, the FGHAZ in the crept condition consists of the lowest fraction of unrecrystallized grains (3.1%) and the highest fraction of fully recrystallized grains (45.1%). The substructured grains, which are in the intermediate state between the unrecrystallized and fully recrystallized, are dominant in all three conditions of the welds.

Kernel average misorientation (KAM) is the arithmetic mean of the scalar misorientations between groups of pixels, or kernels, that measures local strain levels of the grains (Ref. 29). Figure 15 illustrates the local misorientation distribution in the FGHAZ for the three thermal stages (as-welded, PWHT, and crept) by KAM maps. The blue color stands for a misorientation of 0 deg (lowest deformation) and the red color stands for a misorientation of 3 deg (highest deformation). The as-welded FGHAZ shows a relatively higher local misorientation in Fig. 15A. Furthermore, grain boundaries have a higher deformation and misorientation. After PWHT, the unrecrystallized grains are tempered and recovered, resulting in a lower degree of deformation and misorientation in Fig. 15B. Some intersections of grain boundaries still show a relatively higher misorientation. After the creep test, the matrix is further tempered to give the lowest misorientation, but the regions close to the cavities still show a high misorientation — Fig. 15C. The statistical kernel average misorientation distribution is shown in Fig. 16. Relative frequency peak of AW-FGHAZ shifts to higher misorientation values. Crept-FGHAZ obtains the largest frequency of low-angle misorientation value.

Figure 17 shows the microstructure evolution of the matrix grains and precipitates before and after the creep test. Firstly, the recovered and recrystallized grains turn to coarse equiaxed grains. Cr-rich $M_{23}C_6$ carbides distribute within some, not all, grains following the PWHT. This uneven distribu-

tion of carbides to some grains is more apparent following creep. In addition, a coarsening of MX carbonitride is observed on HAGBs following creep. Connected MoC/Mo_2C and M_7C_3 carbide GB networks are detected close to the cavities.

Discussion

The microstructure of creep-damaged FGHAZ has the following features. Firstly, the location of the wedge-type cavities that lead to Type IV failure in P91 are in the lower-peak temperature fine-grained heat-affected zone, or the edge of the heat-affected zone adjacent to the base metal. Secondly, these cavities tend to form at the triple points of high-angle grain boundaries that are enriched with coarsened $M_{23}C_6$ carbides and networked MoC/Mo_2C-type and M_7C_3 carbides. Thirdly, the cavities seem to preferentially form between grains that have fully recrystallized and unrecrystallized grains. The first and second features have been well recognized (Refs. 8, 13). The third feature, that the cavities tend to form between grains that are markedly different in misorientation and degree of recrystallization, has not been reported before. Based on the EBSD results, it is believed that this third feature holds the key for an understanding of the first two features.

It is reasonable to assume that under a constant creep stress, the grains that contain precipitates are stronger and will generate a smaller strain, while the recrystallized grains that are free of carbide particles are weaker and will generate a greater strain. Microhardness (103 HV1) at the location with more particle-free grains is lower than that (126 HV1) of the location with more particle-rich grains. Another evidence is the deformation mismatch across grains that are adjacent to creep cavities (Fig. 15C). It is therefore proposed that the mismatch in creep straining in the FGHAZ may contribute to the nucleation of cavities. It has been suggested by Parker that local strain is responsible for cavity formation (Ref. 23). Figure 15C seems to provide the microstructure and straining evidence to support that mechanism.

The formation of a mixed microstructure of stronger (precipitation-containing) grains and weaker (precipitation-free) grains in the fine-grained HAZ is believed to be the result of the welding thermal cycle. The peak temperature for the edge of the fine-grained HAZ is barely above the A_{C3}. Under this peak temperature, austenite has formed, but the carbide particles in the base metal, especially coarse $M_{23}C_6$ and MX carbides, are only partially dissolved in FGHAZ. In the as-welded condition (Fig. 17A), the Cr-rich, fine $M_{23}C_6$ carbides distribute within some, but not all, grains, and those undissolved coarse $M_{23}C_6$ carbides get trapped within PAGs. The MX carbonitrides are identified as V (C, N) in yellow and Nb (C, N) in blue in Fig. 17. Due to the lower diffusivity and smaller concentration of V and Nb, there are not many precipitated V (C, N) and Nb (C, N) carbonitrides. V (C, N) and Nb (C, N) particles stay within martensite laths. It is also notable that some grains are free of carbides that are detectable (if larger than 0.1 μm) by the EBSD at the magnification.

Based on a pseudo binary phase diagram produced with Thermo-Calc (Ref. 11), the A_{c3} temperature is around 850°C for the 9 mass-% Cr steel. The equilibrium phases are a ferrite, γ austenite, $M_{23}C_6$, and MX phases at 900°C. The A_{c3} temperature of the P91 alloy of this study is 925°C, measured by dilatometry for slow heating and air cooling. During PWHT, martensite grains are further tempered and decomposed, as shown in Fig. 17B. There is a significant grain growth. Relatively finer $M_{23}C_6$ carbides concentrate within some specific grains, but coarser $M_{23}C_6$ carbides stay at HAGBs. The majority of V (C, N) and Nb (C, N) carbonitrides distributes at the HAGBs. MoC/Mo_2C and Cr-rich M_7C_3 carbides are also identified and distribute along the HAGBs. Recovery and recrystallization of the martensite laths lead to formation of finer equiaxed ferrite grains. Movement of excess dislocation accelerates the recovery and recrystallization of the matrix grains during creep deformation with the help of applied stress and creep strain (Refs. 34, 35). Increasing ratio of HAGB/LAGB from 0.48 to 1.06, as shown in Fig. 10, indicates the decreasing stability of grain structure when FGHAZ is exposed to the high creep temperature and stress.

Conclusions

Characteristic features of Type IV creep rupture of P91 welds have been investigated by analyzing microstructure evolution in FGHAZ, under continuous thermal histories, as-welded, after PWHT, and after creep test. The main findings are concluded as follows:

a) The as-welded FGHAZ has a microstructure of martensite laths within fine prior austenite grains. The undissolved, Cr-rich $M_{23}C_6$ carbides are distributed on the PAGBs and some lath boundaries. Fine $M_{23}C_6$ carbides nucleate on the PAGBs and internal martensite laths. EBSD GAM and KAM maps of the FGHAZ show the highest fraction of unrecrystallized grains with a high strain level in the as-welded condition.

b) PWHT tempering produces fine equiaxed ferrite grains and coarsened precipitates. The creep test further tempers the martensite, and promotes the grain growth with an increased HAGB/LAGB ratio from 0.48 as welded to 1.06 as crept. Coarsening and segregation of Cr-rich $M_{23}C_6$ carbides in specific grains causes a higher local strain during creep. MX particles coarsen and stabilize on the high angle grain boundaries. Continuous MoC/Mo_2C and M_7C_3 carbide boundary networks on HAGBs weaken the creep strength of GBs. Connected wedge-type cavities on GBs cause the intergranular Type IV rupture with a low entire creep strain and a large local deformation in the transition zone between FGHAZ and ICHAZ.

c) The welding thermal cycles in the ICHAZ and outer edge of the FGHAZ do not have high enough peak temperatures to promote the formation of grains with uniformly distributed precipitates. Instead, the lower peak temperature tends to retain the variations in precipitate distribution in the base metal microstructure. Recrystallization during PWHT seems to have further enhanced the nonuniform distribution of carbides, i.e., the formation of precipitate-rich and precipitate-free grains. It is proposed that the creep strain mismatch between the unrecrystallized grains that seem to contain precipitates and fully recrystallized grains that seem to be precipitate-free promotes the nucleation of initial cavities during creep.

Acknowledgments

This work has been financially sponsored by the U.S. DOE Office of Nuclear Energy's Nuclear Energy University Programs and by the Discovery program of Natural Sciences and Engineering Research Council (NSERC) of Canada.

References

1. Choudhary, B. K., Saroja, S., Bhanu-Sankara Rao, K., and Mannan, S. L. 1999. Creep-rupture behavior of forged, thick section 9Cr-1Mo ferritic steel. *Metallurgical and Materials Transactions A* 30(11): 2825–2834.

2. Shrestha, T., Basirat, M., Charit, I., Potirniche, G. P., and Rink, K. K. 2013. Creep rupture behavior of grade 91 steel. *Materials Science and Engineering A* 565: 382–391.

3. Aghajani, A., Somsen, C., and Eggeler, G. 2009. On the effect of long-term creep on the microstructure of a 12% chromium tempered martensite ferritic steel. *Acta Materialia* 57(17): 5093–5106.

4. Silwal, B., Li, L., Deceuster, A., and Griffiths, B. 2013. Effect of postweld heat treatment on the toughness of heat-affected zone for grade 91 steel. *Welding Journal* 91(3): 80-s to 87-s.

5. Das, C. R., Albert, S. K., Bhaduri, A. K., Srinivasan, G., and Murty, B. S. 2008. Effect of prior microstructure on microstructure and mechanical properties of modified 9Cr–1Mo steel weld joints. *Materials Science and Engineering A* 477: 185–192.

6. Sireesha, M., Sundaresan, S., and Albert, S. K. 2001. Microstructure and mechanical properties of weld fusion zones in modified 9Cr-1Mo steel. *Journal of Materials Engineering and Performance* 10(1): 320–330.

7. Abe, F., Kern, T. U., and Viswanathan, R. 2008. *Creep-Resistant Steels*. Cambridge, Woodhead Publishing.

8. Mayr, P. 2007. *Weldability of Modern 9%Cr Steels for Application in USC Power Plants*. PhD dissertation. Styria, Graz University of Technology.

9. Kou, S. 1987. *Welding Metallurgy*. Hoboken, N.J.: John Wiley & Sons, Inc.

10. Mayr, P., Schlacher, C., and Mitsche, S. 2011. Critical issues with creep-exposed ferritic-martensitic welded joints for thermal power plants. *Proceedings of the IIW International Conference on Global Trends in Joining, Cutting and Surfacing Technology*. eds. D. V. Kulkarni , M. Samant, S. Krishnan, A. De, J. Krishnan, H. D. Patel, and A. K. Bhaduri, pp. 417–425. Narosa Publishing House Pvt Ltd.

11. Sawada, K., Hara, T., Tabuchi, M., Kimura, K., and Kubushiro, K. 2015. Microstructure characterization of heat affected zone after welding in Mod.9Cr–1Mo steel. *Materials Characterization* 101: 106–113.

12. Paddea, S., Francis, J. A., Paradowska, A. M., Bouchard, P. J., and Shibli, I. A. 2012. Residual stress distributions in a P91 steel-pipe girth weld before and after post weld heat treatment. *Materials Science and Engineering A* 534: 663–672.

13. Albert, S. K., Matsui, M., Watanabe, T., Hongo, H., Kubo, K., and Tabuchi, M. 2003. Variation in the type IV cracking behavior of a high Cr steel weld with post weld heat treatment. *International Journal of Pressure Vessels and Piping* 80: 405–413.

14. Liu, Y., Tsukamoto, S., Sawada, K., and Abe, F. 2014. Role of boundary strengthening on prevention of type IV failure in high Cr ferritic heat resistant steels. *Metallurgical and Materials Transactions A* 45(3): 1306–1314.

15. Abe, F. 2008. Precipitate design for creep strengthening of 9% Cr tempered martensitic steel for ultra-supercritical power plants. *Science and Technology of Advanced Materials* 09: 01–15.

16. Yu, X., Babu, S. S., Terasaki, H., Komizo, Y., Yamamoto, Y., and Santella, M. L. 2013. Correlation of precipitate stability to increased creep resistance of Cr–Mo steel welds. *Acta Materialia* 61(6): 2194–2206.

17. Dawson, K. E., Tatlock, G. J., Chi, K., and Barnard, P. 2013. Changes in precipitate distributions and the microstructural evolution of P24/P91 dissimilar metal welds during PWHT. *Metallurgical and Materials Transactions A* 44(11): 5065–5080.

18. Zavaleta Gutiérrez, N., De Cicco, H., Marrero, J., Danón, C. A., and Luppo, M. I. 2011. Evolution of precipitated phases during prolonged tempering in a 9%Cr1% MoVNb ferritic–martensitic steel: Influence on creep performance. *Materials Science and Engineering A* 528: 4019–4029.

19. Laha, K., Chandravathi, K. S., Parameswaran, P., BhanuSankara Rao, K., and Mannan, S. L. 2007. Characterization of microstructures across the heat-affected zone of the modified 9Cr-1Mo weld joint to understand its role in promoting type IV cracking. *Metallurgical and Materials Transactions A* 38(1): 58–68.

20. Francis, J. A., Mazur, W., and Bhadeshia, H. 2006.Type IV cracking in ferritic power plant steels. *Materials Science and Technology* 22(12): 1387–1395.

21. Abson, D. J., and Rothwell, J. S. 2013. Review of type IV cracking of weldments in 9–12%Cr creep strength enhanced ferritic steels. *International Materials Reviews* 58(8): 438–473.

22. Shinozaki, K., and Kuroki, H. 2003. Stress-strain analysis of creep deterioration in heat affected weld zone in high Cr ferritic heat resistant steel. *Materials Science and Technology* 19(9): 1253–1261.

23. Parker, J. 2013. Factors affecting type IV creep damage in grade 91 steel welds. *Materials Science and Engineering A* 578: 430–437.

24. Parker, J. 2014. In-service behavior of creep strength enhanced ferritic steels grade 91 and grade 92 — Part 2 weld issues. *International Journal of Pressure Vessels and Piping* 114: 76–87.

25. AbdEl-Azim, M. E., Ibrahim, O. H., and El-Desoky, O. E. 2013. Long term creep behaviour of welded joints of P91 steel at 650°C. *Materials Science and Engineering A* 560: 678–684.

26. Liu, Y., Tsukamoto, S., Shirane, T., and Abe, F. 2013. Formation mechanism of type IV failure in high Cr ferritic heat-resistant steel-welded joint. *Metallurgical and Materials Transactions A* 44(1): 4626–4633.

27. ASTM standard E139-06, 2006. Standard test methods for conducting creep, creep-rupture, and stress-rupture tests of metallic materials. *ASTM International*, West Conshohocken, Pa., 2006, DOI: 10.1520/E0139-06, *astm.org*.

28. Wright, S. I., Nowell, M. M., and Field, D. P. 2011. A review of strain analysis using electron backscatter diffraction. *Microscopy and Microanalysis* 17: 316–329.

29. Schwartz, A. J., Kumar, M., Adams, B. L., and Field, D. P. 2009. *Electron Backscatter Diffraction in Materials Science*. New York, Springer.

30. Konrad, J., Zaefferer, S., and Raabe, D. 2006. Investigation of orientation gradients around a hard laves particle in a warm-rolled Fe3Al-based alloy using a 3D EBSD-FIB technique. *Acta Materialia* 54(5): 1969–1980.

31. Cho, J. H., Rollett, A. D., Cho, J. S., Park, Y. J., Moon, J. T., and Oh, K. H. 2006. Investigation of recrystallization and grain growth of copper and gold bonding wires. *Metallurgical and Materials Transactions A* 37(1): 3085–3097.

32. Dziaszyk, S., Payton, E. J., Friedel, F., Marx, V., and Eggeler, G. 2010. On the characterization of recrystallized fraction using electron backscatter diffraction: A direct comparison to local hardness in an IF steel using nanoindentation. *Materials Science and Engineering A* 527: 7854–7864.

33. McCabe, R. J., and Teter, D. F. 2006. Analysis of recrystallized volume fractions in uranium using electron backscatter diffraction. *Journal of Microscopy* 223(1): 33–39.

34. Rollett, A., Humphreys, F. J., Rohrer, G. S., and Hatherly, M. 2004. *Recrystallization and Related Annealing Phenomena*. Oxford, Elsevier.

35. Doherty, R. D., Hughes, D. A., Humphreys, F. J., Jonas, J. J., Jensen, D. J., Kassner, M. E., King, W. E., McNelley, T. R., McQueen, H. J., and Rollett, A. D. 1997. Current issues in recrystallization: A review. *Materials Science and Engineering A* 238: 219–274.